



# Type Ib/Ic Supernovae: Effect of Nickel Mixing on the Early-time Color Evolution and Implications for the Progenitors

Sung-Chul Yoon<sup>1,2,3</sup> , Wonseok Chun<sup>1</sup>, Alexey Tolstov<sup>4,5</sup> , Sergey Blinnikov<sup>4,6,7</sup>, and Luc Dessart<sup>8</sup> 

<sup>1</sup>Department of Physics and Astronomy, Seoul National University, 08826, Seoul, Republic of Korea; [yoons@astro.snu.ac.kr](mailto:yoons@astro.snu.ac.kr)

<sup>2</sup>Center for Theoretical Physics (CTP), Seoul National University, 08826, Seoul, Republic of Korea

<sup>3</sup>Monash Center for Astrophysics, Monash University, Australia

<sup>4</sup>Kavli Institute for the Physics and Mathematics of the Universe (WPI), The University of Tokyo Institutes for Advanced Study, The University of Tokyo, 5-1-5 Kashiwanoha, Kashiwa, Chiba 277-8583, Japan

<sup>5</sup>The Open University of Japan, 2-11, Wakaba, Mihama-ku, Chiba, Chiba 261-8586, Japan

<sup>6</sup>Institute for Theoretical and Experimental Physics (ITEP), Moscow, 117218, Russia

<sup>7</sup>Space Research Institute of the Russian Academy of Sciences (IKI), Moscow, 117997, Russia

<sup>8</sup>Unidad Mixta Internacional Franco-Chilena de Astronomía (CNRS UMI 3386), Departamento de Astronomía, Universidad de Chile, Camino El Observatorio 1515, Las Condes, Santiago, Chile

Received 2018 October 4; revised 2019 January 18; accepted 2019 January 18; published 2019 February 20

## Abstract

We investigate the effect of mixing of radioactive nickel ( $^{56}\text{Ni}$ ) on the early-time color evolution of Type Ib and Ic supernovae (SNe Ib/Ic) using multigroup radiation hydrodynamics simulations. We consider both helium-rich and helium-poor progenitors. Mixing of  $^{56}\text{Ni}$  is parameterized using a Gaussian distribution function. We find that the early-time color evolution with a weak  $^{56}\text{Ni}$  mixing is characterized by three different phases: initial rapid reddening, blueward evolution due to the delayed effect of  $^{56}\text{Ni}$  heating, and redward evolution thereafter until the transition to the nebular phase. With a strong  $^{56}\text{Ni}$  mixing, the color evolution is characterized by a monotonic reddening. We compare our models with the early-time color evolution of several SNe Ib/Ic (SN 1999ex, SN 2008D, SN 2009jf, iPTF13bvn, SN 1994I, SN 2007gr, SN 2013ge, and 2017ein) and find signatures of relatively weak and strong  $^{56}\text{Ni}$  mixing for SNe Ib and SNe Ic, respectively. This suggests that SNe Ib progenitors are distinct from SN Ic progenitors in terms of helium content and that  $^{56}\text{Ni}$  mixing is generally stronger in the carbon–oxygen core and weaker in the helium-rich envelope. We conclude that the early-time color evolution is a powerful probe of  $^{56}\text{Ni}$  mixing in SNe Ib/Ic.

*Key words:* stars: evolution – stars: massive – supernovae: general

## 1. Introduction

Type Ib and Ic supernovae (SNe Ib/Ic) and their progenitors constitute an important subject of stellar evolution theory (see Yoon 2015, for a recent review). The majority of SNe Ib/Ic belong to a subclass of core-collapse SNe, having a massive star origin as implied by their strong correlation with star formation (e.g., Tsvetkov et al. 2001; van den Bergh et al. 2005; Anderson & James 2009; Hakobyan et al. 2009, 2014; Habergham et al. 2010; Leloudas et al. 2011; Kelly & Kirshner 2012; Sanders et al. 2012; Anderson et al. 2015; Xiao & Eldridge 2015; Graur et al. 2017; Kangas et al. 2017; Maund 2018).

Their event rate is relatively high, amounting to about 25% of the ccSN rate (e.g., Smith et al. 2011; Eldridge et al. 2013; Shivvers et al. 2017). The lack of H I spectral lines implies that the progenitors have lost their hydrogen-rich envelope during the pre-SN evolution by stellar wind and/or binary interaction (e.g., Podsiadlowski et al. 1992; Woosley 1993; Woosley et al. 1995; Wellstein & Langer 1999; Eldridge & Tout 2004; Meynet & Maeder 2005; Eldridge et al. 2008; Yoon et al. 2010, 2017; Georgy et al. 2012). The properties of SN Ib/Ic light curves and spectra imply relatively low ejecta masses (i.e.,  $M_{\text{ejecta}} \simeq 1.0\text{--}4.0 M_{\odot}$ ; e.g., Ensmann & Woosley 1988; Shigeyama et al. 1990; Dessart et al. 2011; Drout et al. 2011; Bianco et al. 2014; Taddia et al. 2015, 2018; Lyman et al. 2016; Prentice et al. 2016), in favor of the binary scenario for their progenitors (Yoon 2015). The optically bright progenitor of the SN Ib iPTF13bvn, which has been recently identified in a pre-SN image (Cao et al. 2013; Folatelli et al. 2016), is also consistent with binary progenitor models in terms of the progenitor mass

and optical brightness (Bersten et al. 2014; Eldridge et al. 2015; Kim et al. 2015; Fremling et al. 2016; McClelland & Eldridge 2016; Hirai 2017; Yoon et al. 2017; see also Yoon et al. 2012).

The exact nature of SN Ib/Ic progenitors is still a matter of debate. One outstanding question is what distinguishes type Ib from type Ic progenitors.

Supernovae Ib/Ic are distinguished by the presence or absence of He I lines. Because of this reason, SN Ic progenitors are often regarded as helium-poor stars in the literature. However, the absence of He I lines in SN Ic spectra does not necessarily serve as evidence for the deficiency of helium in SN Ic progenitors. This is because the formation of He I lines by nonthermal processes (Lucy 1991; Swartz 1991) is sensitively affected by the presence of radioactive  $^{56}\text{Ni}$ , and hence by the degree of  $^{56}\text{Ni}$  mixing in SN ejecta (Woosley & Eastman 1997; Dessart et al. 2012). He I lines can be easily formed if  $^{56}\text{Ni}$  were fully mixed in the SN ejecta but a large amount of helium ( $M_{\text{He}} \gtrsim 1.0 M_{\odot}$ ) could be effectively hidden in the spectra with a very weak  $^{56}\text{Ni}$  mixing (Woosley & Eastman 1997; Dessart et al. 2012; Hachinger et al. 2012). For an understanding of the nature of SN Ib/Ic progenitors, therefore, it would be very useful if the  $^{56}\text{Ni}$  distribution in SN Ib/Ic ejecta could be constrained by observations.

The effects of  $^{56}\text{Ni}$  mixing on SN Ib/Ic light curves and spectra have been studied by several authors (Woosley & Eastman 1997; Ensmann & Woosley 1988; Shigeyama et al. 1990; Dessart et al. 2012, 2015, 2016; Bersten et al. 2013; Piro & Nakar 2013). It is found that some degree of  $^{56}\text{Ni}$  mixing is needed not only for the efficient formation of He I lines in the spectra (Woosley & Eastman 1997; Dessart et al.

**Table 1**  
Input Model Properties

Name	$M_{\text{ej}}$ ( $M_{\odot}$ )	$R$ ( $R_{\odot}$ )	$M_{\text{CO}}$ ( $M_{\odot}$ )	$M_{\text{He,env}}$ ( $M_{\odot}$ )	$m_{\text{He}}$ ( $M_{\odot}$ )	$M_{\text{Fe}}$ ( $M_{\odot}$ )	$M_{\text{ext}}$ ( $M_{\odot}$ )
HE3.87	2.40	6.73	2.15	1.72	1.66	1.47	2.7(−5)
CO3.93	2.49	0.77	3.91	0.02	0.10	1.44	5.2(−4)
CO2.16	0.71	0.13	2.16	0.00	0.06	1.46	3.2(−4)

**Note.**  $M_{\text{ej}}$ : ejecta mass (i.e., total mass minus the mass cut);  $M_{\text{CO}}$ : CO core mass;  $M_{\text{He,env}}$ : helium-rich envelope mass;  $m_{\text{He}}$ : integrated helium mass;  $M_{\text{Fe}}$ : iron core mass, which also corresponds to the adopted mass cut for the piston-driven explosion in STELLA;  $M_{\text{ext}}$ : mass of the external buffer used to limit the maximum ejecta velocity (see Section 2 for a discussion). Numbers in parenthesis denote powers of 10.

2012) but also for explaining the overall shape of SN Ib light curves during the post-maximum phase (Shigeyama et al. 1990). The early-time light curve is also found to be significantly affected by the  $^{56}\text{Ni}$  distribution. For example, the post-breakout plateau of a short duration (a few to several days) that is commonly found in the models with a relatively weak  $^{56}\text{Ni}$  mixing disappears with a strong  $^{56}\text{Ni}$  mixing (Ensmann & Woosley 1988; Dessart et al. 2011, 2012; Piro & Nakar 2013).

In addition, larger  $^{56}\text{Ni}$  content in the outermost layers would lead to a higher temperature of the SN Ib/Ic photosphere at very early times, resulting in a bluer color for a given progenitor structure (Piro & Nakar 2013; Dessart et al. 2015)—a similar effect results for an extended progenitor (Nakar & Piro 2014; Dessart et al. 2018). This implies that we can use this information to constrain the degree of  $^{56}\text{Ni}$  mixing in SNe Ib/Ic but this possibility has not been properly explored yet. In this study, we present new multicolor light-curve models of SN Ib/Ic calculated with the STELLA code (Blinnikov et al. 1998, 2000, 2006) and systematically investigate the effects of  $^{56}\text{Ni}$  mixing on the early-time evolution of SNe Ib/Ic. We show that the early-time color evolution of SN Ib/Ic sensitively depends on the  $^{56}\text{Ni}$  distribution, and can be a powerful probe of  $^{56}\text{Ni}$  mixing in SN Ib/Ic.

This paper is organized as follows. In Section 2, we present our progenitor models, the numerical method, and the physical parameters adopted for SN calculations. In Section 3, we present the multicolor light curves of our models. We discuss the effect of  $^{56}\text{Ni}$  mixing on the early-time color evolution in Section 4. We compare our models with several observed SNe Ib/Ic including SN 1994I, SN 1999ex, SN 2007gr, SN 2008D, SN 2009jf, iPTF13bvn, SN 2013ge, and 2013ein in Section 5. We discuss the implications of our results for SNe Ib/Ic progenitors and  $^{56}\text{Ni}$  mixing in Section 6. We conclude our study in Section 7.

## 2. Physical Assumptions and Numerical Method

### 2.1. Input Models

We consider both helium-rich and helium-poor progenitors. These models are constructed with the MESA code (Paxton et al. 2011, 2013, 2015, 2018). In Table 1, we present the properties of our progenitor models. The boundary between the helium-rich envelope and the carbon–oxygen (CO) core is defined by the condition that the mass fraction of helium in the envelope is higher than 0.1. The name starting with “HE” refers

to the helium-rich model, which has an integrated helium mass (i.e.,  $m_{\text{He}} = \int X_{\text{He}} dM_r$ ) of about  $1.7 M_{\odot}$ , and thus is a potential SN Ib progenitor. Note that with this much helium, He I lines would be seen at early times even without nonthermal effects (Dessart et al. 2011). The name with “CO” refers to the helium-poor model ( $m_{\text{He}} \leq 0.1 M_{\odot}$ ), which is almost a naked CO core and can be considered an SN Ic progenitor. The number given in each model name refers to the total mass of the progenitor at the pre-SN stage.

Model HE3.87 is from the binary star model sequence Sm13p50 of Yoon et al. (2017), where the primary star of  $13.0 M_{\odot}$  starts its evolution in a 50 day orbit with a  $11.7 M_{\odot}$  companion. The calculation of this model is stopped when the central temperature reaches  $10^9$  K in Yoon et al. (2017), and the evolution is further followed up to the pre-SN stage for the present study. Model CO2.16 has the same progenitor model and the same adopted physics as model HE3.87 but the mass-loss rate is artificially enhanced (i.e.,  $\dot{M} = 10^{-4} M_{\odot} \text{ yr}^{-1}$ ) after core helium exhaustion, in order to remove the helium-rich envelope. Model CO3.93 is evolved from a pure helium star of  $7.0 M_{\odot}$  at solar metallicity, which would have a  $\sim 20 M_{\odot}$  main-sequence progenitor. Overshooting on top of the helium-burning core is treated as a step function with an overshoot parameter of  $0.1 H_p$  ( $H_p$  is the pressure scale height at the boundary of the convective core). The standard mass-loss prescription for Wolf–Rayet (WR) stars by Nugis & Lamers (2000) is adopted until core helium exhaustion and an enhanced mass-loss rate of  $\dot{M} = 10^{-4} M_{\odot} \text{ yr}^{-1}$  is applied thereafter until the pre-SN stage to remove the helium-rich envelope.

We assume that the mass cut in the ccSN explosion corresponds to the iron core mass  $M_{\text{Fe}}$ , which is the innermost region above which the silicon mass fraction is higher than 0.1. We put  $0.07 M_{\odot}$  of  $^{56}\text{Ni}$  by hand in the progenitor model assuming a Gaussian distribution. The degree of  $^{56}\text{Ni}$  mixing is parameterized using the parameter  $f_m$ , defined as

$$X_{\text{Ni}}(M_r) = A \exp\left(-\left[\frac{M_r - M_{\text{Fe}}}{f_m(M_{\text{tot}} - M_{\text{Fe}})}\right]^2\right), \quad (1)$$

where  $M_r$  is the Lagrangian mass at radius  $r$ , and  $X_{\text{Ni}}$  denotes the mass fraction of  $^{56}\text{Ni}$  at  $M_r$ . The total mass of  $^{56}\text{Ni}$  for a given  $f_m$  is determined by the normalization factor  $A$ . The mass fractions of the other elements are scaled to preserve a normalization of the total mass fraction to unity at each depth. We consider  $f_m = 0.15, 0.3, 0.5, 0.9,$  and  $5.0$ . As shown in Figure 1,  $^{56}\text{Ni}$  is more evenly distributed with a larger value of  $f_m$ . Mixing of the other elements, which is not considered in this study, is potentially important for the early-time light curves of helium-rich models because mixing of carbon and oxygen into the helium-rich envelope can influence the opacity at the SN photosphere. For example, the importance of ionization in the opacity would be reduced with more carbon and oxygen. This effect will be addressed elsewhere.

Our progenitor models are compact ( $R = 6.73 R_{\odot}, 0.77 R_{\odot},$  and  $0.13 R_{\odot}$  for HE3.87, CO3.93, and CO2.16, respectively; Table 1), and the density decreases sharply at the outermost layers (Figure 2). This would make the shock velocity rapidly accelerate to a value close to the speed of light, while our version of the STELLA code does not include relativistic effects. To

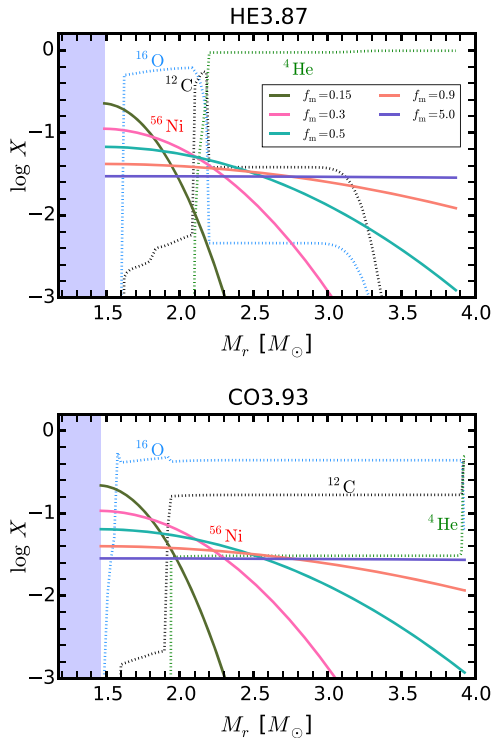


**Figure 1.** Chemical composition in the input models HE3.87 (upper panel) and CO3.93 (lower panel).  $^{56}\text{Ni}$  profiles with  $f_m = 0.15, 0.3, 0.5, 0.9,$  and  $5.0$  according to Equation (1) are color coded.

avoid numerical errors that this high shock velocity can introduce, we add a small amount of external material beyond the stellar surface (i.e., which also mimics the presence of an atmosphere or wind), so that the velocity of the shock front remains significantly below the speed of light. This mass buffer is assumed to have a wind density profile (i.e.,  $\rho = \dot{M}/4\pi v_w r^2$ ) for which the standard  $\beta$ -law for the wind velocity  $v_w$  with  $\beta = 2.0$ ,  $v_\infty = 10 \text{ km s}^{-1}$  and  $\dot{M} = 10^{-3} M_\odot \text{ yr}^{-1}$  is assumed. The maximum radius of this external material is set to  $10^{13} \text{ cm}$  initially (Figure 2). Because CO3.93 and CO2.16 are much more compact, the density decrease at the outer boundary is too sharp and causes too small a time step before shock breakout. Therefore we remove  $\sim 10^{-6} M_\odot$  from the original progenitor model and attach the mass buffer as shown in Figure 2. With this configuration, the ejecta velocity at the outer boundary remains lower than about  $4 \times 10^4 \text{ km s}^{-1}$  in all of our SN models. Although this external structure is unrealistic, its mass is very small (i.e.,  $M_{\text{ext}} \lesssim 5 \times 10^{-4} M_\odot$ ; Table 1) and it affects the SN light curves only for a short period ( $< 1$  day) after shock breakout.

## 2.2. Supernova Models

We use the STELLA code for calculating our SN models. STELLA is a one-dimensional Lagrangian multigroup (i.e., energy dependent) radiation hydrodynamics code (Blinnikov et al. 1998, 2000, 2006) that implicitly solves the time-dependent radiation transfer equation coupled with hydrodynamics. The gamma-ray transfer is solved in a one-group approximation following Ambwani & Sutherland (1988). Positron kinetic energy is absorbed locally (see also Blinnikov et al. 1998). The maximum number of wavelength bins in the code may be up to 1000, but has been fixed to 100 in our simulations, which covers from  $5 \times 10^4$  to  $10^{-3} \text{ \AA}$  in principle.

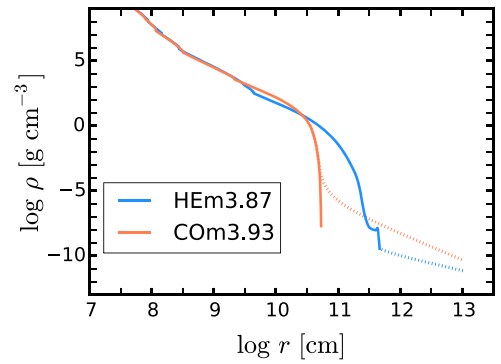


**Figure 2.** Density profiles of the input models HE3.87 (orange) and CO3.93 (skyblue). The solid and dotted lines give the density profiles of the progenitor models and the attached external material, respectively. See the text for details.

In most cases, the shortest wavelength considered in the calculations is about  $0.1 \text{ \AA}$ . This is suitable to properly describe nonequilibrium continuum radiation. The ionization is obtained from a solution to the Saha equation (i.e., it assumes local thermodynamic equilibrium; LTE).

Our input models are mapped into the STELLA code using a grid of 200–300 mass zones. The explosion is applied by a thermal bomb at the mass cut with an explosion energy of 1.0, 1.5, and 1.8 B.

We summarize the properties of the bolometric luminosity of our SN models with  $M_{\text{Ni}} = 0.07 M_\odot$  in Table 2 and those of  $U$ -,  $B$ -,  $V$ -, and  $R$ -band magnitudes in Table 3. The input model, the mixing parameter (i.e.,  $f_m$ ), and the explosion energy are indicated in the SN model names of the tables. For example, HE3.87\_fm0.15\_E1.5 means that the input model is HE3.87 and that the adopted mixing parameter and explosion energy are  $f_m = 0.15$  and  $E_{\text{exp}} = 1.5 \text{ B}$ , respectively. For a given explosion energy  $E_{\text{exp}}$ , the resultant kinetic energy of the SN ( $E_K$ ) is lower by about 0.3 B for HE3.87 and 0.4 B for CO3.93 and CO2.12 (Table 2), which correspond to the binding energy above the mass cut in the progenitor models.

In the next two sections, we focus our discussion on the SN models with HE3.87 and CO3.93. The behavior of the SN models with CO2.12 according to different degrees of  $^{56}\text{Ni}$  mixing is qualitatively similar to that of CO3.93 and we present the results with CO2.12 only for the comparison with observations, which is discussed in Section 5 below.

## 3. Light Curves

From Table 2, we confirm the following well-known facts about SN Ib/Ic. (1) The rise time from the shock breakout to the bolometric peak ( $t_{\text{max}}$ ) and the light-curve width (i.e.,  $\delta t_{\text{Bol},+1/2} + \delta t_{\text{Bol},-1/2}$ ) become systematically smaller for a higher explosion energy for a given  $f_m$ . (2) The bolometric luminosity at its peak ( $L_{\text{Bol,max}}$ ) increases with a higher explosion energy for a given  $f_m$ .

Figures 3 and 4 present the light curves and the evolution of photospheric properties of HE3.87 SN models with  $E_{\text{exp}} = 1.5 \text{ B}$ . The photosphere of an SN Ib/Ic is not well defined (see Section 7 of Dessart et al. 2015) and in Figure 4 we present properties at the optical depth of  $2/3$  that is defined with the Rosseland-mean opacity. In Figure 3, the shock breakout corresponds to the initial spike in the bolometric light curves. The subsequent evolution is affected by the  $^{56}\text{Ni}$  distribution.

**Table 2**  
Properties of Bolometric Light Curves of the SN Models with  $M_{\text{Ni}} = 0.07 M_{\odot}$

Name	$E_K$ (B)	$L_{\text{Bol,max}}$ ( $10^{42}$ erg $\text{s}^{-1}$ )	$t_{\text{Bol,max}}$ (days)	$\delta t_{\text{Bol,-1/2}}$ (days)	$\delta t_{\text{Bol,+1/2}}$ (days)	$M_{\text{Bol,max}}$ (mag)
HE3.87_fm0.15_E1.0	0.67	1.69	23.82	9.56	14.91	-16.85
HE3.87_fm0.3_E1.0	0.67	1.67	23.08	9.13	15.86	-16.84
HE3.87_fm0.5_E1.0	0.69	1.64	22.11	11.02	14.21	-16.82
HE3.87_fm0.9_E1.0	0.69	1.62	21.14	13.31	12.70	-16.81
HE3.87_fm5.0_E1.0	0.69	1.61	18.08	12.21	14.19	-16.80
HE3.87_fm0.15_E1.5	1.17	1.80	19.41	6.98	15.50	-16.92
HE3.87_fm0.3_E1.5	1.17	1.81	18.94	7.47	14.18	-16.93
HE3.87_fm0.5_E1.5	1.18	1.83	18.00	8.57	13.18	-16.94
HE3.87_fm0.9_E1.5	1.19	1.82	17.33	10.12	11.35	-16.93
HE3.87_fm5.0_E1.5	1.19	1.77	14.94	9.80	12.32	-16.90
HE3.87_fm0.15_E1.8	1.47	1.85	18.07	6.83	15.03	-16.95
HE3.87_fm0.3_E1.8	1.47	1.85	17.99	7.76	14.75	-16.95
HE3.87_fm0.5_E1.8	1.48	1.89	17.51	8.82	12.07	-16.98
HE3.87_fm0.9_E1.8	1.49	1.85	15.00	8.65	12.51	-16.95
HE3.87_fm5.0_E1.8	1.49	1.84	15.29	10.47	9.96	-16.94
CO3.93_fm0.15_E1.0	0.57	1.64	30.85	11.42	15.34	-16.82
CO3.93_fm0.3_E1.0	0.58	1.53	29.19	13.16	16.96	-16.75
CO3.93_fm0.5_E1.0	0.58	1.45	26.02	13.51	20.20	-16.69
CO3.93_fm0.9_E1.0	0.58	1.40	23.16	15.06	23.04	-16.65
CO3.93_fm5.0_E1.0	0.58	1.36	17.44	11.74	27.88	-16.62
CO3.93_fm0.15_E1.5	1.07	1.87	24.93	9.74	19.73	-16.97
CO3.93_fm0.3_E1.5	1.08	1.79	24.86	12.08	18.85	-16.91
CO3.93_fm0.5_E1.5	1.08	1.70	22.10	11.04	19.43	-16.86
CO3.93_fm0.9_E1.5	1.08	1.62	18.97	11.85	18.99	-16.81
CO3.93_fm5.0_E1.5	1.08	1.55	15.32	10.25	21.27	-16.76
CO3.93_fm0.15_E1.8	1.37	1.99	23.20	9.70	18.49	-17.03
CO3.93_fm0.3_E1.8	1.38	1.88	21.52	8.98	18.50	-16.97
CO3.93_fm0.5_E1.8	1.38	1.78	21.23	11.18	16.96	-16.91
CO3.93_fm0.9_E1.8	1.38	1.70	17.91	11.25	16.80	-16.86
CO3.93_fm5.0_E1.8	1.38	1.61	15.04	10.22	18.80	-16.80
CO2.12_fm0.15_E1.0	0.60	2.20	11.78	5.62	12.91	-17.14
CO2.12_fm0.3_E1.0	0.60	2.27	11.44	5.81	14.09	-17.18
CO2.12_fm0.5_E1.0	0.60	2.20	12.07	6.22	12.23	-17.14
CO2.12_fm0.9_E1.0	0.60	2.10	11.00	6.36	12.03	-17.09
CO2.12_fm5.0_E1.0	0.60	2.03	10.05	6.35	11.49	-17.05

**Note.**  $E_K$ : kinetic energy of SN,  $L_{\text{Bol,max}}$ : bolometric luminosity at the main peak,  $t_{\text{Bol,max}}$ : time from the shock breakout to the main peak of the bolometric luminosity,  $\delta t_{\text{Bol,-1/2}}$ : time span from  $L_{\text{Bol,max}}/2$  to  $L_{\text{Bol,max}}$ ,  $\delta t_{\text{Bol,+1/2}}$ : time span from  $L_{\text{Bol,max}}$  to  $L_{\text{Bol,max}}/2$ ,  $M_{\text{Bol,max}}$ : bolometric magnitude at the main peak.

With a relatively weak mixing of  $^{56}\text{Ni}$  (i.e.,  $f_m = 0.15$  and  $0.3$ ), a post-breakout plateau that lasts for several days is observed. This short phase is commonly observed in SN Ib/Ic models with weak or no  $^{56}\text{Ni}$  mixing (Ensmann & Woosley 1988; Shigeyama et al. 1990; Dessart et al. 2011) and is powered by the release of shock deposited energy (from both radiation and internal gas energy, i.e., ionization energy from helium, carbon, and oxygen) as the temperature decreases continuously. Readers are referred to Dessart et al. (2011) for a detailed discussion on this post-breakout plateau. The plateau phase comes to an end when the photosphere reaches down to the region heated by  $^{56}\text{Ni}$  at about 6 days (the upper panel of Figure 5) and thereafter the bolometric luminosity starts to increase toward the main peak.

In the optical bands, the light curves with a weak  $^{56}\text{Ni}$  mixing ( $f_m = 0.15$  and  $0.3$ ) have double peaks (Figure 3). The first peak, which is associated with the early post-breakout evolution, is fainter than the main peak by about 1.6–2.4 mag, depending on the band. Note that this magnitude difference

between the first and main peaks (in the optical) would become larger for a higher  $^{56}\text{Ni}$  mass (which leads to a brighter main peak; e.g., Ensmann & Woosley 1988), or for a smaller radius of the progenitor envelope (which leads to a fainter first peak; e.g., Ensmann & Woosley 1988; Dessart et al. 2011, 2018).

For a stronger  $^{56}\text{Ni}$  mixing ( $f_m \geq 0.5$ ), the post-breakout plateau practically disappears (see also Dessart et al. 2012). As shown in Figure 4, the mass fraction of  $^{56}\text{Ni}$  at the photosphere immediately after the shock breakout is already greater than  $10^{-3}$  for  $f_m \geq 0.5$  and  $^{56}\text{Ni}$  heating plays the dominant role in the luminosity evolution (see the lower panel of Figure 5; Dessart et al. 2012, 2015). The time span from the shock breakout to the luminosity peak ( $t_{\text{Bol,max}}$  in Table 2) becomes shorter with a stronger  $^{56}\text{Ni}$  mixing, while the light-curve width defined by the full width at half maximum (i.e., FWHM  $\equiv \delta t_{\text{Bol,+1/2}} + \delta t_{\text{Bol,-1/2}}$ ) tends to increase instead.

In the experiment of Dessart et al. (2012), He I lines were present if the local mass fraction of  $^{56}\text{Ni}$  was greater than about 0.01 in the helium-rich layers. In the HE3.87 models, this



**Table 3**  
Properties of  $U$ -,  $B$ -,  $V$ -,  $R$ -band Light Curves of SN Models with  $M_{\text{Ni}} = 0.07 M_{\odot}$

Name	$U_{\text{max}}$	$t_{U_{\text{max}}}$	$\delta t_{U,-1/2}$	$B_{\text{max}}$	$t_{B_{\text{max}}}$	$\delta t_{B,-1/2}$	$V_{\text{max}}$	$t_{V_{\text{max}}}$	$\delta t_{V,-1/2}$	$R_{\text{max}}$	$t_{R_{\text{max}}}$	$\delta t_{R,-1/2}$
HE3.87_fm0.15_E1.0	-16.71	21.79	6.42	-16.64	22.79	7.42	-17.08	24.55	9.18	-17.27	24.55	10.29
HE3.87_fm0.3_E1.0	-16.43	21.37	7.42	-16.53	21.37	7.42	-17.10	23.08	9.13	-17.33	24.33	10.38
HE3.87_fm0.5_E1.0	-15.94	19.13	9.10	-16.36	20.73	10.69	-17.12	21.45	10.36	-17.41	23.28	11.09
HE3.87_fm0.9_E1.0	-15.77	10.98	6.87	-16.23	17.70	11.92	-17.12	18.58	10.75	-17.45	21.61	12.70
HE3.87_fm5.0_E1.0	-16.03	9.18	6.11	-16.28	11.20	6.79	-17.13	18.08	11.83	-17.45	19.94	12.27
HE3.87_fm0.15_E1.5	-16.89	18.59	6.16	-16.68	18.59	6.16	-17.12	19.41	6.98	-17.32	20.44	8.01
HE3.87_fm0.3_E1.5	-16.60	16.89	5.42	-16.61	18.32	6.85	-17.18	19.54	8.07	-17.42	20.66	9.19
HE3.87_fm0.5_E1.5	-16.11	16.49	7.98	-16.49	17.05	8.07	-17.23	18.00	8.57	-17.50	19.61	10.18
HE3.87_fm0.9_E1.5	-15.91	11.20	8.16	-16.37	13.82	8.79	-17.24	16.91	9.70	-17.55	17.71	9.48
HE3.87_fm5.0_E1.5	-16.10	7.43	4.36	-16.41	11.87	8.28	-17.23	14.94	9.58	-17.54	16.92	10.54
HE3.87_fm0.15_E1.8	-16.99	16.66	5.41	-16.69	17.31	6.07	-17.12	18.65	7.40	-17.33	19.17	7.92
HE3.87_fm0.3_E1.8	-16.70	15.59	4.89	-16.64	16.78	6.55	-17.19	18.68	7.99	-17.45	20.43	9.74
HE3.87_fm0.5_E1.8	-16.20	14.12	6.04	-16.54	15.77	7.68	-17.26	17.08	8.39	-17.55	18.37	9.16
HE3.87_fm0.9_E1.8	-16.00	10.17	7.08	-16.45	14.06	9.27	-17.27	15.00	8.65	-17.55	16.63	9.77
HE3.87_fm5.0_E1.8	-16.16	7.03	3.94	-16.47	11.08	7.70	-17.26	12.89	7.87	-17.56	15.29	9.28
CO3.93_fm0.15_E1.0	-15.81	27.65	7.21	-16.23	28.69	9.26	-16.92	30.85	11.42	-17.26	30.85	11.42
CO3.93_fm0.3_E1.0	-15.46	24.31	8.27	-16.07	26.36	10.32	-16.89	29.19	13.16	-17.25	30.01	12.96
CO3.93_fm0.5_E1.0	-14.84	19.72	9.92	-15.79	22.76	12.28	-16.85	26.02	14.53	-17.26	26.02	13.51
CO3.93_fm0.9_E1.0	-15.00	10.45	6.47	-15.72	13.54	8.28	-16.80	20.59	14.09	-17.25	23.16	15.06
CO3.93_fm5.0_E1.0	-16.11	9.19	5.88	-16.24	10.56	5.89	-16.87	15.06	9.14	-17.18	21.45	14.56
CO3.93_fm0.15_E1.5	-16.11	21.47	6.29	-16.39	22.21	7.03	-17.07	24.10	8.92	-17.40	24.93	9.74
CO3.93_fm0.3_E1.5	-15.81	19.45	6.67	-16.28	21.50	8.73	-17.07	23.52	10.74	-17.42	24.86	11.05
CO3.93_fm0.5_E1.5	-15.20	17.02	8.00	-16.03	18.50	9.47	-17.04	19.72	9.67	-17.42	22.10	11.04
CO3.93_fm0.9_E1.5	-15.09	10.73	6.85	-15.88	12.54	7.80	-16.99	17.17	11.05	-17.40	18.97	11.85
CO3.93_fm5.0_E1.5	-16.07	7.25	4.01	-16.27	9.03	5.11	-16.99	14.88	9.81	-17.31	17.04	11.08
CO3.93_fm0.15_E1.8	-16.23	20.32	5.74	-16.45	21.08	7.57	-17.14	23.20	9.70	-17.46	23.20	9.70
CO3.93_fm0.3_E1.8	-15.91	18.47	5.93	-16.33	19.06	6.52	-17.14	21.52	8.98	-17.46	21.52	8.98
CO3.93_fm0.5_E1.8	-15.33	16.15	8.08	-16.11	17.41	8.34	-17.10	18.47	8.42	-17.46	21.76	11.71
CO3.93_fm0.9_E1.8	-15.17	9.59	5.60	-15.95	13.02	8.35	-17.04	15.38	9.15	-17.44	17.91	10.69
CO3.93_fm5.0_E1.8	-16.08	7.16	4.12	-16.29	9.04	5.29	-17.03	13.72	8.90	-17.34	16.13	10.55
CO2.16_fm0.15_E1.0	-17.41	10.31	4.14	-16.97	11.78	5.62	-17.23	13.58	7.41	-17.41	13.58	7.41
CO2.16_fm0.3_E1.0	-17.38	9.51	3.88	-17.03	11.14	5.50	-17.34	13.11	6.47	-17.50	15.15	8.50
CO2.16_fm0.5_E1.0	-16.88	9.01	3.17	-16.94	9.83	3.98	-17.46	12.07	6.22	-17.62	13.06	7.22
CO2.16_fm0.9_E1.0	-16.40	7.95	3.82	-16.78	9.09	4.69	-17.47	11.00	6.14	-17.68	11.33	6.02
CO2.16_fm5.0_E1.0	-16.32	6.82	3.75	-16.72	8.06	4.63	-17.44	9.74	5.61	-17.69	10.73	6.31

**Note.**  $U_{\text{max}}$ ,  $B_{\text{max}}$ ,  $V_{\text{max}}$ ,  $R_{\text{max}}$ :  $U$ -,  $B$ -,  $V$ -, and  $R$ -band magnitudes at maximum,  $t_{U_{\text{max}}}$ ,  $t_{B_{\text{max}}}$ ,  $t_{V_{\text{max}}}$ ,  $t_{R_{\text{max}}}$ : time from the shock breakout to the  $U$ -,  $B$ -,  $V$ -, and  $R$ -band maximum,  $\delta t_{U,-1/2}$ ,  $\delta t_{B,-1/2}$ ,  $\delta t_{V,-1/2}$ ,  $\delta t_{R,-1/2}$ : time span from the half maximum to the maximum (i.e., the time needed for a brightness increase by 0.75 mag to maximum) in  $U$ -,  $B$ -,  $V$ -, and  $R$ -bands.

condition is met with  $f_m \geq 0.3$  at the optical maximum, for which the supernova would appear as an SN Ib. The exact level of  $^{56}\text{Ni}$  for the production of He I lines would depend on the ejecta mass and helium-shell mass.

Figure 4 shows that the photosphere (defined here with the Rosseland-mean opacity) is systematically located further out (in radius, velocity, or Lagrangian mass) for a larger  $f_m$ . This is mainly because of the change in ionization caused by the extra heating in the outermost layers of the ejecta for a higher  $^{56}\text{Ni}$  abundance.

The helium-deficient SN models with CO3.93 presented in Figure 6 have qualitatively similar properties to those of HE3.87. With  $f_m = 0.15$  and  $0.3$ , the post-breakout plateau is developed as in the case of HE3.87. Double peak features are also seen in the optical. The initial radius of CO3.93 ( $R = 0.77 R_{\odot}$ ) is much smaller than that of HE3.87 ( $R = 6.73 R_{\odot}$ ) and the first peaks in the optical are fainter by a factor of a few than those of HE3.87. The photosphere in CO3.93 models is systematically located further outward than in HE3.87 models

(Figures 4 and 7). The FWHM of the bolometric light curve for a given set of  $f_m$  and  $E_{\text{exp}}$  is also larger in CO3.93 models (Table 2), although the CO3.93 and HE3.87 models have similar kinetic energy and ejecta mass.

#### 4. Color Evolution

We present the  $B-V$  and  $V-R$  color evolution of our HE3.87 and CO3.93 SN models with  $E_{\text{exp}} = 1.5 B$  and  $M_{\text{Ni}} = 0.07 M_{\odot}$  in Figures 8 and 9. Here the color evolution is shown only from 0.05 day after the shock breakout because the shock breakout features, which are practically unobservable in the optical, make the figure somewhat difficult to read clearly. The initial evolution is characterized by the rapid increase of  $B-V$  and  $V-R$  (i.e., the SN reddens) for all the considered  $f_m$  values. This represents the initial cooling phase due to rapid expansion with no heating source.

This initial rapid reddening phase is followed by a slope change and the subsequent evolution is affected by the  $^{56}\text{Ni}$

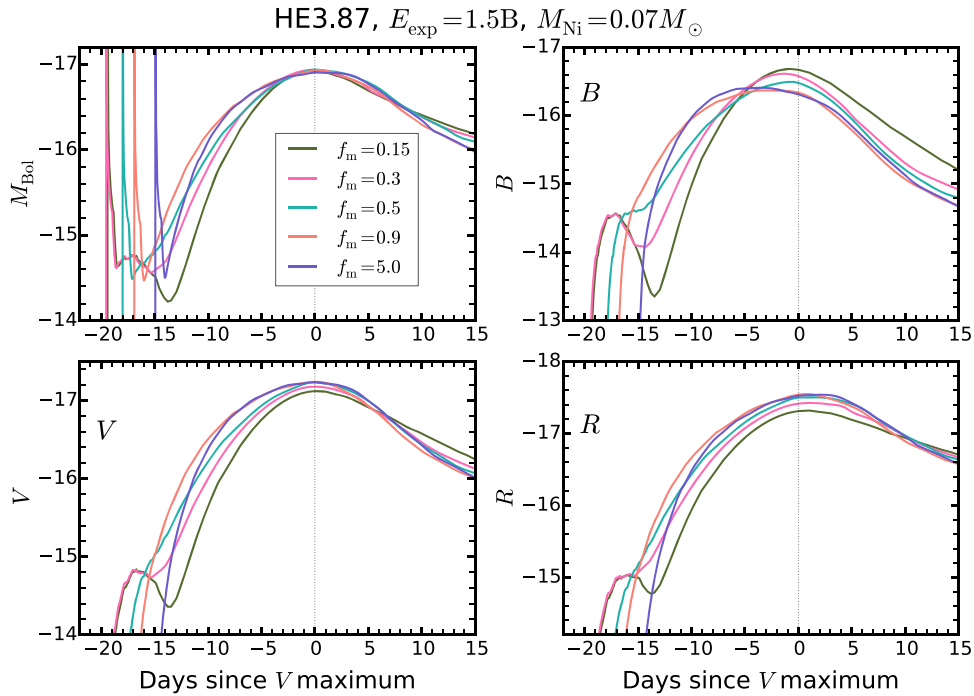


**Figure 3.** Light curves of bolometric,  $B$ -,  $V$ - and  $R$ -band magnitudes of HE3.87 SN models with an explosion energy of 1.5 B and a  $^{56}\text{Ni}$  mass of  $0.07 M_{\odot}$ . The results with  $f_m = 0.15, 0.3, 0.5, 0.9,$  and  $5.0$  are presented using different colors as indicated by the legends in the upper left panel.

distribution. For a weak  $^{56}\text{Ni}$  mixing ( $f_m = 0.15$  and  $0.3$ ), the color turns blueward at  $t \simeq -14$  days and  $-18$  days with respect to the  $V$ -band maximum for HE3.87 and CO3.93, respectively, because of the delayed effect of  $^{56}\text{Ni}$  heating. This sign change of the slope in the color curves marks the end point of the post-breakout plateau phase and the beginning of the rebrightening shown in Figures 3 and 6. This color change in weak mixing models is also implied by the temperature evolution in Figures 4 and 7, where the photospheric temperature rapidly decreases initially and starts to increase again. The color curves reach a local minimum several days before the  $V$ -band maximum and the models continue to redden thereafter until the nebular phase. Observations show that the color becomes blue again  $\sim 10$  days after the optical maximum as the SN enters the nebular phase (e.g., Stritzinger et al. 2018). This phase cannot be properly described by the STELLA code because the LTE approximation for the gas breaks down (see Dessart et al. 2015, 2016).

For a very strong mixing of  $^{56}\text{Ni}$  ( $f_m = 0.9$  and  $5.0$ ), the dominant role of  $^{56}\text{Ni}$  heating makes the initial reddening due to rapid expansion much weaker and the sign of the color curve slope does not change: the color continues to redden monotonically. For  $f_m = 0.5$ , which is the intermediate case between weak/extreme mixing, the magnitude differences after the initial reddening remain nearly constant until a few days before the  $V$ -band maximum and increase thereafter.

In Figure 10, we compare the  $B-V$  evolution of HE3.87 models for different explosion energies. A lower explosion energy leads to a longer rise time to the optical maximum and to a slightly redder color at the first peak of  $B-V$ , which marks the end of the initial rapid cooling phase. The color at the  $V$ -band maximum is not significantly affected by the explosion energy either. The figure shows that a larger amount of  $^{56}\text{Ni}$  may make the SN color systematically bluer, which results from more significant  $^{56}\text{Ni}$  heating, but the overall behavior of the color evolution is not affected by the total amount of  $^{56}\text{Ni}$ .

We conclude that the slope change of the color curve is mainly determined by the  $^{56}\text{Ni}$  distribution. This means that the color evolution before the optical maximum would provide a strong observational constraint on  $^{56}\text{Ni}$  mixing in SN Ib/Ic as discussed below.

## 5. Comparison with Observations

We have shown that the  $^{56}\text{Ni}$  distribution in SN Ib/Ic ejecta impacts their optical color evolution during the photospheric phase. Here we confront our models with several observed SNe Ib/Ic. We do not intend to quantitatively infer physical parameters like the ejecta kinetic energy and mass, the  $^{56}\text{Ni}$  mass, or the progenitor radius of each SN. Instead we focus our discussion on the color evolution in a qualitative way.

The observed  $B-V$  color of our SN Ib/Ic sample is systematically bluer than the model predictions. This difference might be attributed to different  $^{56}\text{Ni}$ /ejecta masses, uncertainties in the reddening correction, non-LTE effects that are not included in our STELLA models, or our mixing procedure (which affects only the  $^{56}\text{Ni}$  distribution). Observations indicate significant asphericity in ordinary SNe Ib/Ic (e.g., Maund et al. 2007; Tanaka et al. 2008, 2012, 2017; Reilly et al. 2016) and multidimensional effects might also play an important role for the color evolution.

### 5.1. Type Ib Supernovae

On the left side of Figure 11, we present the  $V$ -band light curves and  $B-V$  color curves of four different SNe Ib (i.e., SN 1999ex, SN 2008D, SN 2009jf, and iPTF13bvn), compared with our HE3.87 SN models with  $E_{\text{exp}} = 1.0$  B and  $M_{\text{Ni}} = 0.07 M_{\odot}$ . These SNe Ib are very good test cases of our model predictions because they were observed from about 20 to 15 days before the  $V$ -band maximum.

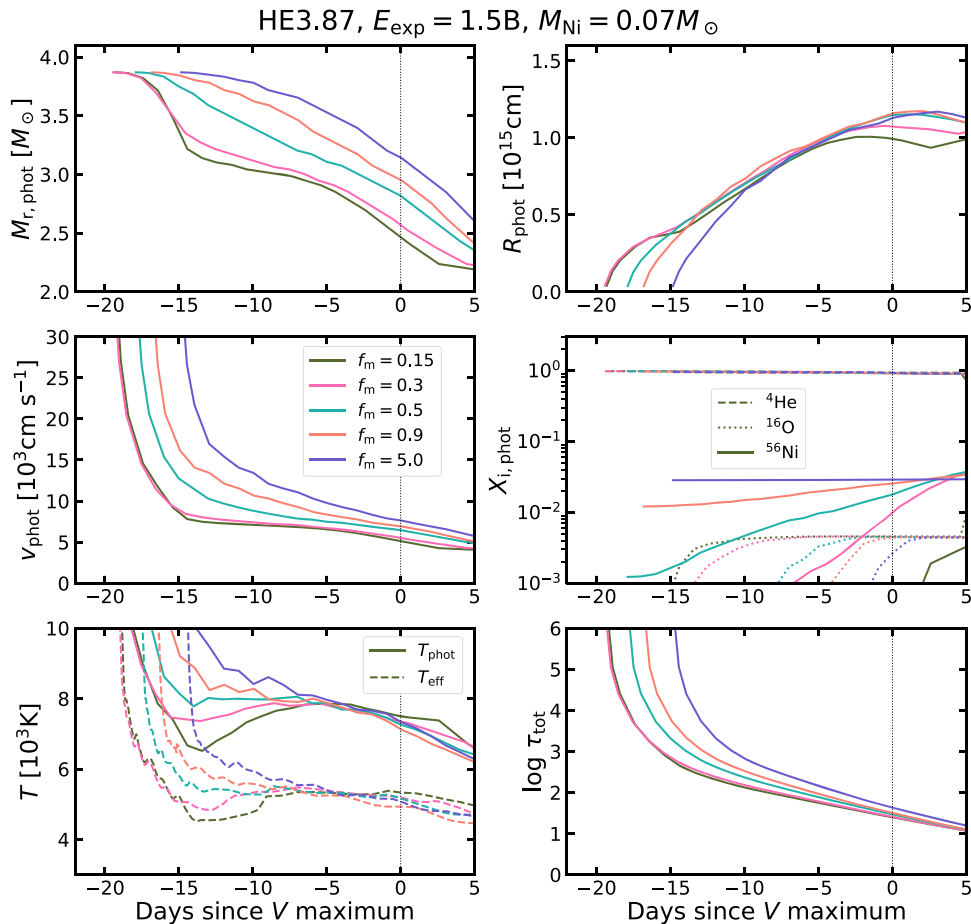


**Figure 4.** Evolution of the photospheric properties of HE3.87 SN models with an explosion energy of 1.5 B and a  $^{56}\text{Ni}$  mass of  $0.07 M_{\odot}$ : mass coordinate (top-left), radius (top-right), velocity (middle-left), chemical composition (middle-right), gas temperature (bottom-left) at the photosphere. The mass coordinate in the top-left panel includes the iron core mass in the progenitor (hence the neutron star remnant mass after SN explosion). The photosphere is defined as the position where the optical depth is  $2/3$  calculated using the Rosseland-mean opacity. In the bottom-left panel, the effective temperatures defined by the Stefan–Boltzmann law are also given by the dotted lines for comparison. The bottom right panel gives the total optical depth of the ejecta calculated using the Rosseland-mean opacity. The results with  $f_m = 0.15, 0.3, 0.5, 0.9,$  and  $5.0$  are presented using different colors as indicated by the legends in the middle-left panel.

### 5.1.1. SN 1999ex

The most remarkable case is SN 1999ex. As shown in the figure, the initial rapid reddening phase is unambiguously observed for a period of  $t \simeq -20 \cdots -17$  days with respect to the  $V$ -band maximum. Then the  $B-V$  color reddens until about  $t = -10$  days before becoming blue again. Here, this behavior is matched by our weak mixing model (e.g.,  $f_m = 0.15$ ), implying that the  $^{56}\text{Ni}$  distribution in the SN 1999ex ejecta is highly concentrated in the center. The double peak feature predicted in weak mixing models (Figure 3) is not found in the  $B$ -,  $V$ - and  $R$ - band light curves. However, Stritzinger et al. (2002) reports a strong signature of the post-breakout plateau in the  $U$ - band for this SN. It is likely that the first peak in the other optical bands was missed in the SN survey because it was too faint (i.e., fainter by  $>4$  mag than at the optical maximum as implied by Figure 11). As discussed in Section 3, the magnitude difference between the first and main peaks in the optical can be much larger than what is predicted by the HE3.87 SN models for a higher  $^{56}\text{Ni}$  mass and/or for a more compact progenitor (e.g., Dessart et al. 2018). A more detailed study should explain the lack of an optical post-breakout plateau in a quantitative way.

Hamuy et al. (2002) classify SN 1999ex as Type Ib/c instead of Type Ib, arguing that it is an intermediate case

between Ib and Ic. This is because helium lines in the optical are relatively weak compared to those of ordinary SNe Ib. The weak  $^{56}\text{Ni}$  mixing evidenced by the color evolution of SN 1999ex implies that the weakness of He I lines is not necessarily due to a relatively small amount of helium. Note also that He I lines of this SN gradually become stronger as the light curve approaches its main peak as in the case of ordinary SNe Ib (Hamuy et al. 2002). This is consistent with the case of weak  $^{56}\text{Ni}$  mixing in a helium-rich ejecta where thermal processes form weak He I lines initially and in later stages nonthermal processes due to radioactive decay of  $^{56}\text{Ni}$  gradually become more important to make stronger He I lines (Dessart et al. 2012).

We conclude that the progenitor of SN 1999ex might have retained a fairly large amount of helium and that the relative weakness of He I lines are not necessarily due to a small content of helium.

### 5.1.2. iPTF13bvn

The color evolution in Figure 11 indicates that the initial rapid reddening phase is missing for iPTF13bvn. However, we observe that the color reddens from  $t = -18$  days until about  $t = -13$  days with respect to the  $V$ -band maximum and becomes bluer thereafter until  $t = -7$  days with respect to the

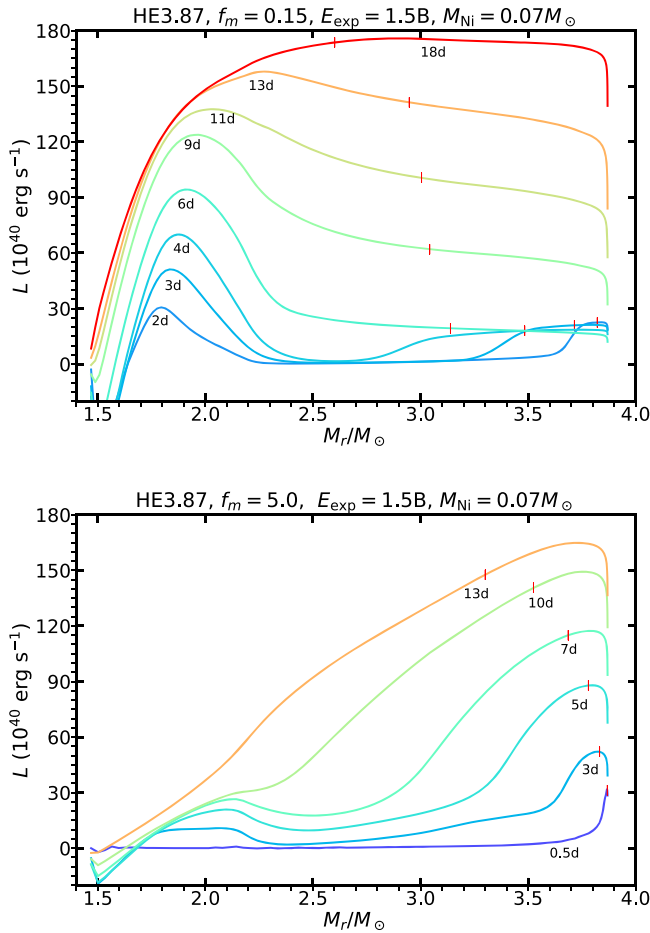


**Figure 5.** Evolution of the luminosity profile in the models HE3.87\_fm0.15\_E1.5 (upper panel) and HE3.87\_fm5.0\_E1.5 (lower panel). The label in each line denotes days since explosion. The vertical red line in each profile gives the position of the photosphere defined with the Rosseland-mean opacity.

$V$ -band maximum. This provides evidence for a relatively weak  $^{56}\text{Ni}$  mixing. The difference in the strength of He I lines between iPTF13bvn and SN 1999ex would have resulted from somewhat different degrees of  $^{56}\text{Ni}$  mixing (see Dessart et al. 2012). For example, both HE3.87 SN models with  $f_m = 0.15$  and  $f_m = 0.3$  have a similar qualitative slope change in the color evolution (Figure 8), but the influence of  $^{56}\text{Ni}$  radioactive decay at the photosphere for the formation of He I lines would become more important with  $f_m = 0.3$  as implied by the evolution of the chemical composition at the photosphere presented in Figure 4.

### 5.1.3. SN 2009jf

Early-time data is available for SN 2009jf (i.e.,  $V - V_{\text{max}} \simeq 4$  mag; Figure 11). The initial rise in the light curve from  $V - V_{\text{max}} \simeq 4$  mag to  $V - V_{\text{max}} \simeq 3$  mag is very rapid but a small decrease in the slope is observed from  $V - V_{\text{max}} \simeq 3$  to  $V - V_{\text{max}} \simeq 2.4$  mag. This behavior is qualitatively similar to the HE3.87 SN model prediction with  $f_m = 0.5$ . The color evolution is also qualitatively consistent with the prediction with  $f_m = 0.5$ , although the model prediction is much redder than the observation. Unfortunately, however, the  $B - V$  data is missing for  $t \simeq -19 \dots -17$  days with respect to the  $V$ -band maximum, and we do not know how strong the initial

reddening was. This makes it difficult to precisely determine which model is most consistent with the color evolution of this SN.

### 5.1.4. SN 2008D

SN 2008D is an SN Ib with very luminous post-breakout emission (Soderberg et al. 2008; Malesani et al. 2009; Modjaz et al. 2009). Bersten et al. (2013) invoked jet-induced  $^{56}\text{Ni}$  mixing into high-velocity outermost layers of the ejecta to explain the early-time evolution of this SN. More recently, Dessart et al. (2018) argued that the featureless spectra having weak He I lines during early times can be better explained by a helium-giant progenitor having an extended and tenuous envelope (i.e.,  $R \sim 200 R_{\odot}$ ). The post-breakout plateau phase is rather short (i.e., about 3 days) and is followed by an increase in luminosity toward the main peak.

In the lower panel of Figure 11 we see that SN 2008D does not become as red as SN 1999ex at the end of the initial reddening phase (i.e.,  $B - V = 0.5 - 0.6$  mag at  $t \simeq -13$  days for SN 2008D compared to  $B - V \simeq 0.1$  mag at  $t \simeq -17$  days for SN 1999ex). In the context of our study on  $^{56}\text{Ni}$  mixing, this would imply a stronger mixing in SN 2008D than in SN 1999ex, although not as extreme as assumed by Bersten et al. (2013). This property of relatively strong ejecta mixing may be compatible with the giant progenitor model proposed by Dessart et al. (2018), which is crucial to explain the large early-time brightness. Indeed, in the helium-giant scenario, chemical mixing induced by the Rayleigh–Taylor instability would be more efficient (Shigeyama et al. 1990; Hachisu et al. 1991). Subsequently, the color behavior is quite similar to the other events and very strong mixing (i.e.,  $f_m = 0.9 - 5.0$ ) is ruled out.

## 5.2. Type Ic Supernovae

The properties of ordinary SNe Ic, as we understand them today, are similar to those of SNe Ib in terms of kinetic energy, ejecta mass, and  $^{56}\text{Ni}$  mass in general. The observed sample is heterogeneous, with a greater diversity for SNe Ic relative to SNe Ib. For example, SN 1994I, which is the prototype of SNe Ic, has an unusually short rise time. Furthermore, all SNe associated with long gamma-ray bursts (GRB) and all hydrogen-deficient hyper-energetic/superluminous SNe have been found to belong to Type Ic (Woosley & Bloom 2006; Gal-Yam 2012; Branch & Wheeler 2017). So far, there is no SN Ib associated with a long GRB or hyper-energetic/superluminous SN, with the possible exceptions of SN 2016coi, which exhibits unusually broad He I lines (Yamanaka et al. 2017), and of SN 2005bf, whose high luminosity may be powered by a magnetar (e.g., Maeda et al. 2007). The origin of the SN Ic diversity is currently poorly known. Rapid core rotation in the SN progenitor may be a necessary condition for making a central engine (either collapsar or magnetar) susceptible to power a hyper-energetic/superluminous SN (Woosley 1993; Wheeler et al. 2000). Given that our 1D STELLA models cannot be directly compared to these peculiar SNe Ic, whose ejecta are probably highly asymmetric (e.g., Maeda et al. 2003; Dessart et al. 2017), our discussion is limited to SNe Ic that appear to be ordinary in terms of kinetic energy ( $E_K = 1 \sim 2$  B) and  $^{56}\text{Ni}$  mass ( $M_{\text{Ni}} \approx 0.1 M_{\odot}$ ).

On the right side of Figure 11 our CO3.93 SN models with  $E_{\text{exp}} = 1.8$  B and  $M_{\text{Ni}} = 0.07 M_{\odot}$  are compared with SN



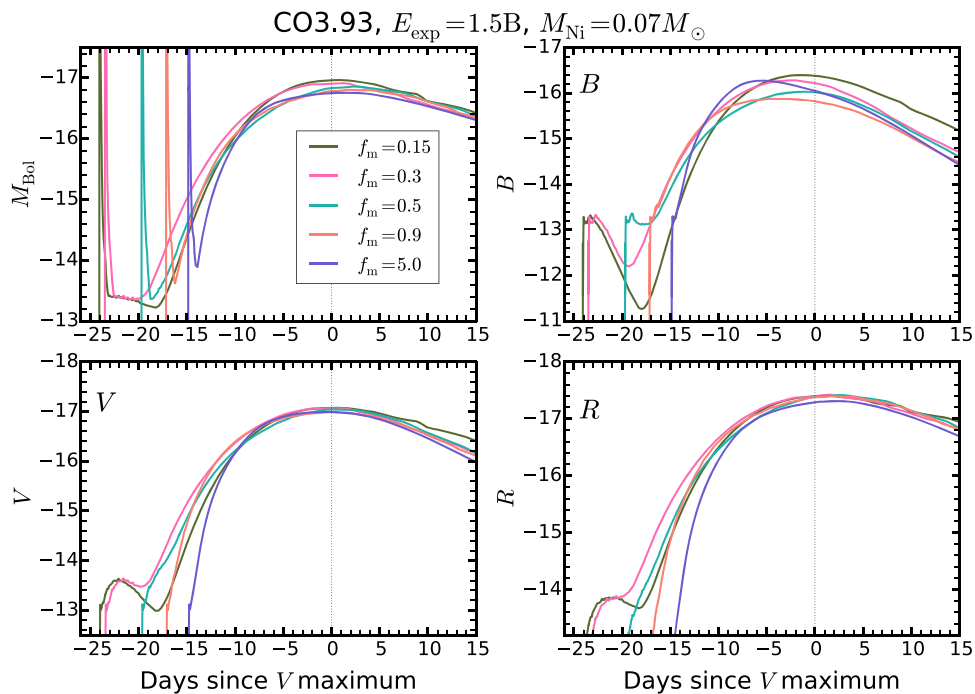


Figure 6. Same as in Figure 3 but for CO3.93 SN models.

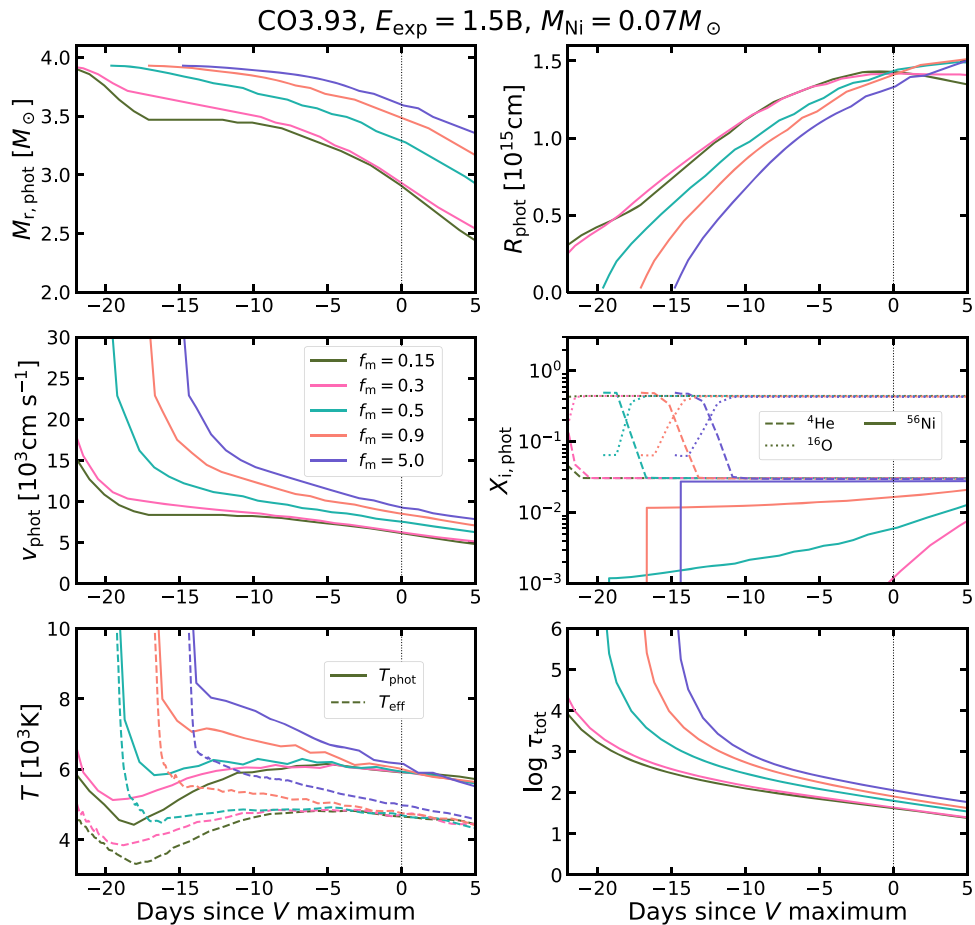
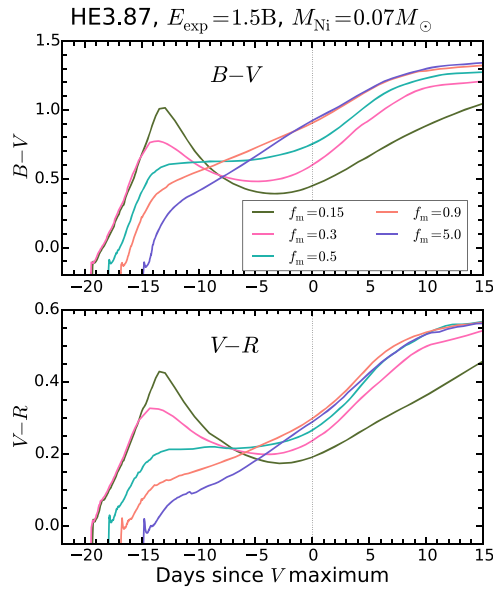
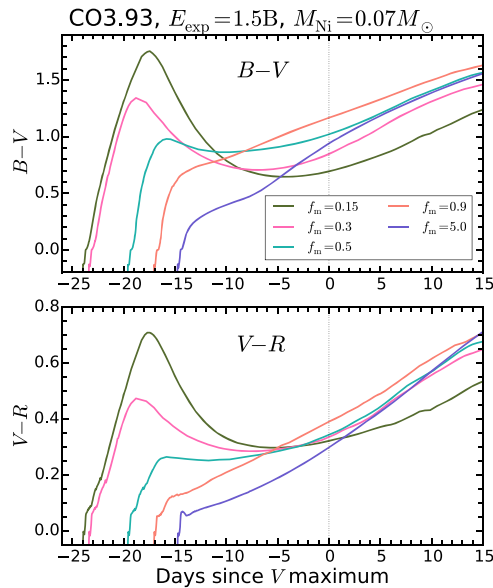


Figure 7. Same as in Figure 4 but for CO3.93 SN models.



**Figure 8.** Evolution of  $B-V$  (upper panel) and  $V-R$  (lower panel) colors of HE3.87 SN models with an explosion energy of 1.5 B and a  $^{56}\text{Ni}$  mass of  $0.07 M_{\odot}$  since 0.05 days after the shock breakout. The results with  $f_m = 0.15, 0.3, 0.5, 0.9,$  and  $5.0$  are given by different colors as indicated by the legends in the upper panel.



**Figure 9.** Same as in Figure 8 but for CO3.93 SN models.

1994I, SN 2007gr, SN 2013ge, and SN 2017ein. The early-time features of these SNe are relatively well studied compared to those of other SNe Ic. The first data for SN 1994I is very deep ( $V - V_{\text{max}} \approx 3.0$ ) but for the other three SNe Ic, we have only  $V - V_{\text{max}} \approx 1.0$  at the first data point, which is much smaller than in the case of SNe Ib (i.e.,  $V - V_{\text{max}} \gtrsim 2.0$  at the first data point). Therefore, our argument presented below for these three SNe Ic is weaker than in the case of SNe Ib.

There is no clear evidence for He I lines in the optical spectra of SN 1994I, SN 2007gr and SN 2017ein, which have been classified as Type Ic. Drout et al. (2016) report weak He I lines in the early optical spectra of SN 2013ge and classify this SN as SN Ib/c. However, unlike SN 1999ex, these He I signatures

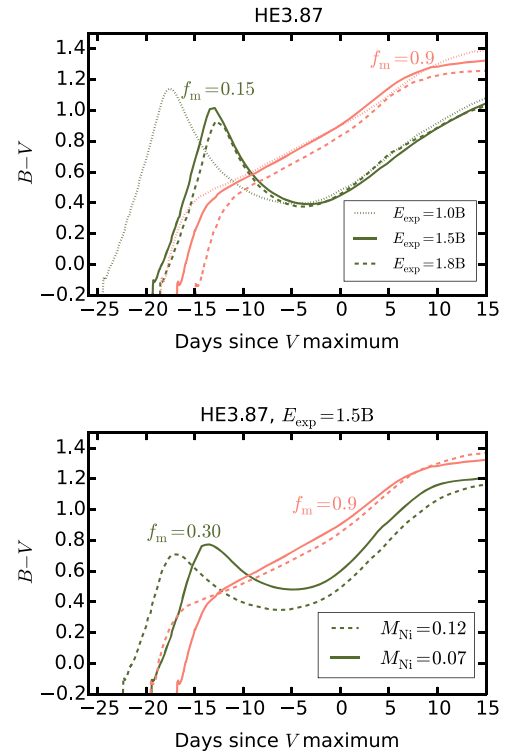


**Figure 10.** Upper panel: the  $B-V$  color evolution of HE3.87 SN models with a  $^{56}\text{Ni}$  mass of  $0.07 M_{\odot}$  and with  $f_m = 0.15$  (green) and  $0.90$  (orange) for three different explosion energies:  $E_{\text{exp}} = 1.0$  (dotted),  $1.5$  (solid), and  $1.8$  (dashed) B. Lower panel: the  $B-V$  color evolution of HE3.87 SN models with an explosion energy of  $1.5$  B and with  $f_m = 0.3$  (green) and  $0.9$  (orange) for two different  $^{56}\text{Ni}$  masses:  $M_{\text{Ni}} = 0.07$  (solid line) and  $M_{\text{Ni}} = 0.12$  (dashed line).

soon disappear and SN 2013ge would have been classified as SN Ic without early-time spectra. This suggests that signatures of helium could have been observed in many other SNe Ic if data at earlier times had been available. The color evolution of SN 2013ge, which shows a monotonic increase in  $B-V$ , is qualitatively different from the SNe Ib discussed above but similar to SN 1994I.

The ejecta masses of SN 2007gr, SN 2013ge, and SN 2017ein are inferred to be about  $2-3 M_{\odot}$  (Valenti et al. 2008; Mazzali et al. 2010; Drout et al. 2016; Van Dyk et al. 2018), which is comparable to that of the CO3.93 model. A caveat is that these estimates based on the light curves are subject to uncertainties (e.g., Dessart et al. 2016). Nondetection with a very deep limit is reported 5 and 7 days before the discovery of SN 2007gr and SN 2013ge, respectively (Valenti et al. 2008; Drout et al. 2016). SN 1994I has a very low ejecta mass (i.e.,  $M_{\text{ej}} \approx 0.6-1.0 M_{\odot}$ ; e.g., Iwamoto et al. 1994; Nomoto et al. 1994; Sauer et al. 2006) that leads to a much narrower light curve than those of SN 2007gr and SN 2013ge. The first detection of SN 1994I is likely to be within a few days from explosion (Richmond et al. 1996).

### 5.2.1. SN 1994I and SN 2013ge

As shown in Figure 11 (the bottom right panel), the  $B-V$  value of SN 1994I and SN 2013ge monotonically increases from the first detection. Given that the time span between the nondetection and the discovery of these SNe is fairly short ( $<1-2$  days for SN 1994I and  $<5$  days for SN 2013ge), it is unlikely that the signature of delayed  $^{56}\text{Ni}$  heating (i.e., a decrease of  $B-V$  after the initial reddening phase) could have

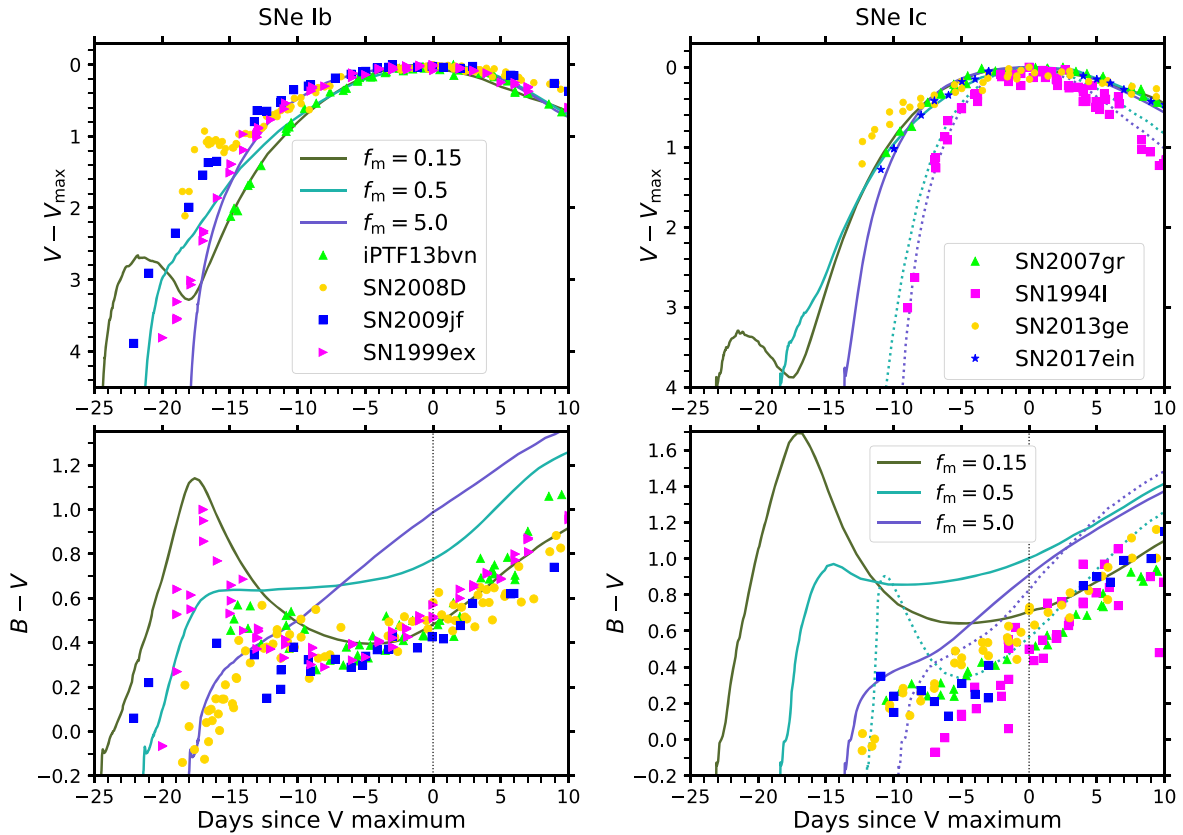


**Figure 11.** Upper left panel:  $V$ -band light curves with  $V_{\max}$  of iPTF13bvn, SN 2008D, SN 2009jf, and SN 1999ex compared with HE3.87 SN models with  $E_{\text{exp}} = 1.0$  B and  $M_{\text{Ni}} = 0.07 M_{\odot}$ . Upper right panel: SN 2007gr, SN 2013ge, and SN 2017ein compared with CO3.93 SN models with  $E_{\text{exp}} = 1.8$  B and  $M_{\text{Ni}} = 0.07 M_{\odot}$  (solid line), and SN 1994I compared with CO2.16 models with  $E_{\text{exp}} = 1.0$  B and  $M_{\text{Ni}} = 0.07 M_{\odot}$  (dotted line). Lower panel: the corresponding  $B-V$  color curves. The SN data are taken from the Open Supernova Catalog (<https://sne.space>) except SN 2007gr and SN 2017ein of which the data are from Chen et al. (2014) and Van Dyk et al. (2018), respectively. Reddening correction ( $E(B-V)$ ) is applied for each SN as the following. iPTF13bvn: 0.12 (Fremling et al. 2016), SN 2008D: 0.6 (Soderberg et al. 2008; Modjaz et al. 2009), SN 2009jf: 0.16 (Valenti et al. 2011), SN 1999ex: 0.28 (Stritzinger et al. 2002), SN 2007gr: 0.085 (Chen et al. 2014), SN 1994I: 0.45 (Richmond et al. 1996), SN 2013ge: 0.067 (Drout et al. 2016), and SN 2017ein: 0.34 (Van Dyk et al. 2018).

been present before the discovery. Therefore, the color evolution implies that  $^{56}\text{Ni}$  is almost fully mixed in the ejecta of these SNe. This contrasts with the case of SNe Ib, for which the color behavior points to a relatively weak  $^{56}\text{Ni}$  mixing.

As shown by Hachinger et al. (2012) and Dessart et al. (2012), not much helium could be hidden in SNe Ic if  $^{56}\text{Ni}$  were strongly mixed in the ejecta.<sup>9</sup> Therefore, our analysis leads to the conclusion that the progenitors of SN 1994I and SN 2013ge did not have a helium-rich envelope, being an almost naked carbon–oxygen core.

### 5.2.2. SN 2007gr and SN 2017ein

For SN 2007gr, the  $B-V$  color curve is somewhat flat for  $t = -10 \dots -5$  days with respect to the  $V$ -band maximum, and it seems to be compatible with the case of  $f = 0.5$ . Given the lack of earlier data for this SN; however, we cannot well constrain the degree of  $^{56}\text{Ni}$  mixing based on the color evolution.

SN 2017ein has a weak signature of the effect of delayed  $^{56}\text{Ni}$  heating on the  $B-V$  color curve (i.e., the slight decrease of  $B-V$  during  $t = -12 \dots -10$  days with respect to the  $V$ -band maximum). This indicates that  $^{56}\text{Ni}$  mixing in this SN was

<sup>9</sup> The value  $m_{\text{He}} < \sim 0.2 M_{\odot}$  has been proposed for SN 1994I, for which a very low ejecta mass has been inferred, but the situation is probably more complicated in general. The presence of He I lines may also depend on the CO core mass, the local He mass fraction, the level of chemical segregation, etc.

weaker than in SN 1994I and SN 2013ge. Although the lack of He I lines around the  $V$ -band maximum might be due to weak  $^{56}\text{Ni}$  mixing, the constraint set on He is weak given the lack of spectra within  $\sim 5$  days of explosion. At such times, He I lines may be produced even without nonthermal effects if the progenitor had a massive helium-rich envelope with a very high helium mass fraction (i.e.,  $X_{\text{He}} \gtrsim 0.9$ ; Dessart et al. 2011).

## 6. Implications for SN Ib/Ic Progenitors and Nickel Mixing

We schematically summarize our discussion of the previous section in Figure 12. We tentatively conclude that the color evolution of SNe Ib differs from that of SNe Ic because of different  $^{56}\text{Ni}$  distributions in the ejecta. For SNe Ib, strong mixing of  $^{56}\text{Ni}$  into the helium-rich envelope is ruled out and only relatively weak/moderate mixing can be compatible with observations, while very weak mixing is also ruled out as otherwise no He I lines would form at the optical maximum. For some SNe Ic (i.e., SN 1994I and SN 2013ge),  $^{56}\text{Ni}$  seems to be strongly mixed throughout the SN ejecta, implying that the progenitors of these SNe Ic are intrinsically helium poor as otherwise helium could not be hidden in the spectra.

From this finding, we suggest the following propositions regarding SN Ib/Ic progenitors and  $^{56}\text{Ni}$  mixing in SNe, which need to be tested by future studies:

1. Progenitors of SNe Ib and SNe Ic do not form a continuous sequence in terms of helium content in

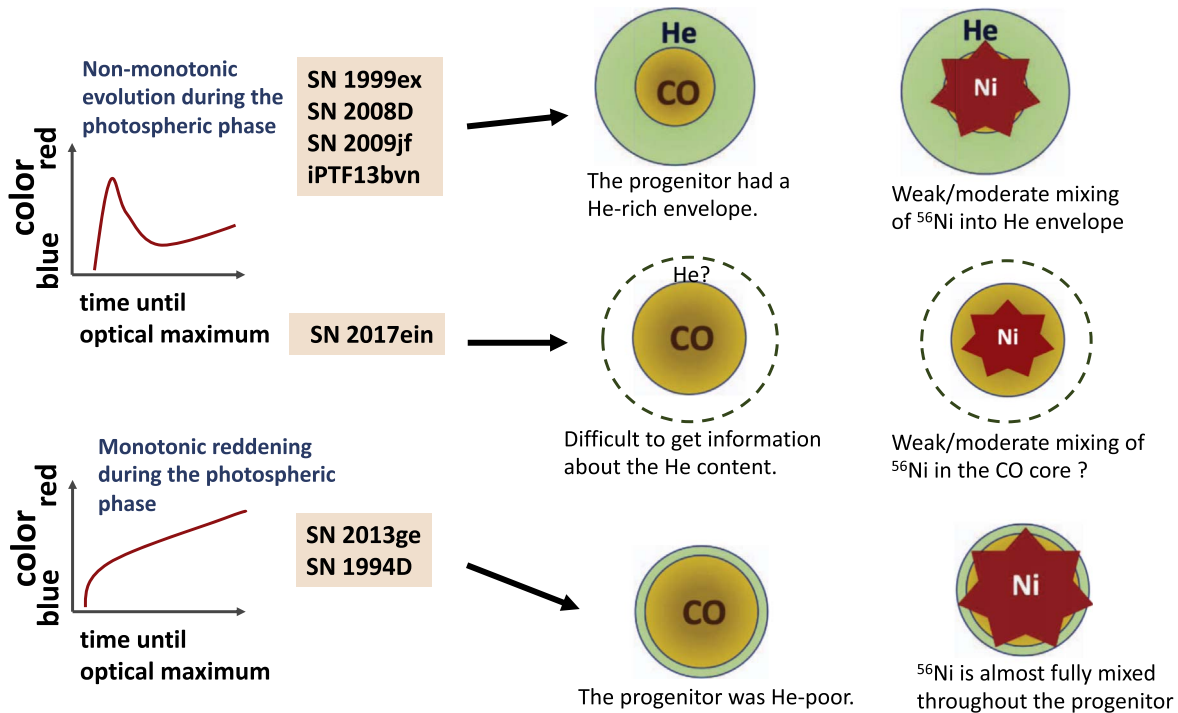


Figure 12. Schematic summary of our discussion in Section 5.

general. They differ for most cases meaning that SNe Ib progenitors have a helium-rich envelope with a high mass fraction of helium ( $\gtrsim 0.9$ ) and SNe Ic progenitors are almost naked CO cores that only have a small amount of helium left in the outermost layers with a low mass fraction of helium.

- Mixing of  $^{56}\text{Ni}$  into the CO core during the explosion is very efficient irrespective of SN type. Hence, type Ic SNe, whose progenitors are naked CO cores, exhibit a monotonic (optical) color evolution until the nebular phase, which is a signature of strong  $^{56}\text{Ni}$  mixing.
- In progenitors that have a helium-rich envelope, mixing of  $^{56}\text{Ni}$  from the CO core into the helium envelope induced by hydrodynamic instabilities is probably weaker, depending on the progenitor structure.

The first proposition needs to be confronted by the predictions of stellar evolution theory. Type Ib/Ic SN progenitor models by Yoon et al. (2010) predict that the total helium mass in SN Ib/Ic progenitors decreases in a continuous way as a function of the initial mass. This is a consequence of the adopted mass-loss rate prescription for WR stars given by Hamann et al. (1995) that depends only on the luminosity and the surface hydrogen abundance. Recently, Yoon (2017) revisited the mass-loss rate prescription of WR stars. He found that the helium mass distribution in SN Ib/Ic progenitors would be bimodal, i.e., either larger than about  $1.0 M_{\odot}$  or less than about  $0.2 M_{\odot}$  depending on the initial mass of the progenitors, if the mass-loss enhancement during the WC stage of WR stars compared to the case of WN stage was properly taken into account. Therefore, the first proposition is supported by the conclusion of Yoon (2017).<sup>10</sup>

<sup>10</sup> SNe Ic like SN 1994I have a very small ejecta mass ( $M_{\text{ej}} \lesssim 1.0 M_{\odot}$ ). Mass transfer from naked helium stars during core carbon burning in close binary systems (so-called Case BB) would play an important role for their progenitors (Nomoto et al. 1994; Wellstein & Langer 1999; Yoon et al. 2010; Tauris et al. 2015).

This is also consistent with the recent observations that indicate systematic differences between SNe Ib and Ic in spectral properties (Liu et al. 2016; Prentice & Mazzali 2017). For example, it is found that SNe Ic have a stronger absorption line O I  $\lambda 7774$  and higher velocities of Fe II  $\lambda 5169$  and O I  $\lambda 7774$  than SNe Ib (Liu et al. 2016).

The second proposition seems to be well supported by various multidimensional simulations where efficient  $^{56}\text{Ni}$  mixing into the CO core is often observed (e.g., Kifonidis et al. 2003, 2006; Hammer et al. 2010; Ono et al. 2013; Mao et al. 2015; Wongwathanarat et al. 2017; Müller et al. 2018). Recently Taddia et al. (2018) found that SNe Ic light curves are particularly well fitted by models with a significant  $^{56}\text{Ni}$  mixing, which also supports the second proposition.

Mixing of  $^{56}\text{Ni}$  into the helium envelope would depend on the progenitor structure as discussed by Shige-yama et al. (1990) and Hachisu et al. (1991). Using 2D numerical simulations, Hachisu et al. (1991) showed that  $^{56}\text{Ni}$  mixing into the helium envelope due to the R–T instability in an SN progenitor with a helium-rich envelope can become more efficient for lower mass progenitors because of the higher density contrast between the CO core and the helium envelope. Almost complete mixing of  $^{56}\text{Ni}$  into the helium envelope as in the cases of  $f_m = 0.9$  and  $5.0$  of our models (Figure 1) is not found in their simulations. In their  $3.3 M_{\odot}$  helium star model where mixing occurs most efficiently in their calculations,  $^{56}\text{Ni}$  is mixed only up to a middle point of the helium envelope, which is comparable to the cases of  $f_m = 0.3$ – $0.5$  in our calculations. Such moderate mixing is suitable for explaining the color evolution of SN 2008D and SN 2009jf. For  $6 M_{\odot}$  helium star model, on the other hand, the R–T instability is shown to be very weak and mixing occurs only in a limited region around the interface between the CO core and the helium envelope, which may well explain the properties of SN 1999ex. Therefore, the third proposition above is in good agreement with the result of Hachisu et al. (1991). However,



Hachishu et al. did not consider the effects of neutrino-driven convection and  $^{56}\text{Ni}$  fingers that play an important role for chemical mixing in SN ejecta (e.g., Kifonidis et al. 2003). It is also likely that the degree of  $^{56}\text{Ni}$  mixing depends on the ratio of the  $^{56}\text{Ni}$  mass to the SN ejecta mass (i.e., weaker mixing for a lower  $^{56}\text{Ni}$  to ejecta mass ratio). Further systematic investigations of chemical mixing in SNe Ib/Ic with more realistic multidimensional simulations are needed.

## 7. Conclusions

We have discussed the effects of the  $^{56}\text{Ni}$  distribution in SN ejecta on the early-time light curve and color evolution of SNe Ib/Ic. The results presented in Section 3 imply that the presence or absence of an early plateau phase can help constrain the degree of  $^{56}\text{Ni}$  mixing. However, such an early plateau, if present, would be short-lived and much fainter than the main peak and would thus be easily missed. A complementary and more suitable approach is to use the early-time color evolution. We have shown that it can be a sensitive diagnostic of the  $^{56}\text{Ni}$  distribution (Section 4). With a weak  $^{56}\text{Ni}$  mixing, the early-time optical color initially reddens for about a week (radiation and expansion cooling is not compensated by  $^{56}\text{Ni}$  heating in photospheric layers), and subsequently evolves to the blue up to a week before maximum (delayed heating from  $^{56}\text{Ni}$ ), followed by a continuous reddening until the nebular phase. With a strong  $^{56}\text{Ni}$  mixing, the effect of  $^{56}\text{Ni}$  heating is more continuous and progressive, so that the color is initially bluer than in weakly mixed cases and the color reddens slowly and monotonically during the photospheric phase.

We have shown that the relatively weak/moderate  $^{56}\text{Ni}$  mixing feature is found with SN 2008D, SN 2009jf, and iPTF13bvn which belong to Type Ib, while the feature of strong  $^{56}\text{Ni}$  mixing is found with SN 1994I, which belongs to Type Ic. Our result also implies the possibility that SN 2009ex that was considered as an intermediate case (i.e., Type Ib/c) between SN Ib and SN Ic by Hamuy et al. (2002) have relatively weak He I lines because of inefficient  $^{56}\text{Ni}$  mixing into the helium envelope rather than because of small helium content in the progenitor. On the other hand, SN 2013ge is also classified as Type Ib/c based on weak helium signature in the earliest spectra (Drout et al. 2016) but the signature of strong  $^{56}\text{Ni}$  mixing in the color evolution of this SN and the disappearance of helium lines in later stages provide evidence that the progenitor did not have a helium-rich envelope.

We tentatively conclude that the population of SN Ib/Ic progenitors is largely bimodal in terms of helium content (Section 6). For further tests of our conclusions, we suggest future multidimensional numerical simulations of chemical mixing using realistic SN Ib/Ic progenitor models and more observations with detailed case studies of individual SNe Ib/Ic on the early-time evolution.

This work was supported by the Korea Astronomy and Space Science Institute under the R&D program supervised by the Ministry of Science and ICT. S.C.Y. thanks Alexander Heger, Francisco Förster, Alejandro Clocchiatti, Myungshin Im, and Changsu Choi for useful discussions. S.C.Y. acknowledges the support by the Monash Center for Astrophysics via the distinguished visitor program. A.T. and S.B. are supported by the World Premier International Research Initiative (WPI Initiative). S.B. is supported by RSCF grant 18-12-00522 in his

work on the STELLA code development. The work of A.T. is also supported by JSPS KAKENHI grant No. JP16H02166.

*Software:* STELLA (Blinnikov et al. 1998, 2000, 2006), MESA (Paxton et al. 2011, 2013, 2015, 2018).

## ORCID iDs

Sung-Chul Yoon  <https://orcid.org/0000-0002-5847-8096>

Alexey Tolstov  <https://orcid.org/0000-0002-4587-7741>

Luc Dessart  <https://orcid.org/0000-0003-0599-8407>

## References

- Ambwani, K., & Sutherland, P. 1988, *ApJ*, 325, 820
- Anderson, J. P., & James, P. A. 2009, *MNRAS*, 399, 559
- Anderson, J. P., James, P. A., Habergan, S. M., Galbany, L., & Kuncarayakti, H. 2015, *PASA*, 32, e019
- Bersten, M. C., Benvenuto, O. G., Folatelli, G., et al. 2014, *AJ*, 148, 68
- Bersten, M. C., Tanaka, M., Tominaga, N., Benvenuto, O. G., & Nomoto, K. 2013, *ApJ*, 767, 143
- Bianco, F. B., Modjaz, M., Hicken, M., et al. 2014, *ApJS*, 213, 19
- Blinnikov, S., Lundqvist, P., Bartunov, O., Nomoto, K., & Iwamoto, K. 2000, *ApJ*, 532, 1132
- Blinnikov, S. I., Eastman, R., Bartunov, O. S., Popolitov, V. A., & Woosley, S. E. 1998, *ApJ*, 496, 454
- Blinnikov, S. I., Röpke, F. K., Sorokina, E. I., et al. 2006, *A&A*, 453, 229
- Branch, D., & Wheeler, J. C. 2017, *Supernova Explosions* (Berlin: Springer)
- Cao, Y., Kasliwal, M. M., Arcavi, I., et al. 2013, *ApJL*, 775, L7
- Chen, J., Wang, X., Ganeshalingam, M., et al. 2014, *ApJ*, 790, 120
- Dessart, L., Hillier, D. J., Li, C., & Woosley, S. 2012, *MNRAS*, 424, 2139
- Dessart, L., Hillier, D. J., Livne, E., et al. 2011, *MNRAS*, 414, 2985
- Dessart, L., Hillier, D. J., Woosley, S., et al. 2015, *MNRAS*, 453, 2189
- Dessart, L., Hillier, D. J., Woosley, S., et al. 2016, *MNRAS*, 458, 1618
- Dessart, L., John Hillier, D., Yoon, S.-C., Waldman, R., & Livne, E. 2017, *A&A*, 603, A51
- Dessart, L., Yoon, S.-C., Livne, E., & Waldman, R. 2018, *A&A*, 612, A61
- Drout, M. R., Milisavljevic, D., Parrent, J., et al. 2016, *ApJ*, 821, 57
- Drout, M. R., Soderberg, A. M., Gal-Yam, A., et al. 2011, *ApJ*, 741, 97
- Eldridge, J. J., Fraser, M., Maund, J. R., & Smartt, S. J. 2015, *MNRAS*, 446, 2689
- Eldridge, J. J., Fraser, M., Smartt, S. J., Maund, J. R., & Crockett, R. M. 2013, *MNRAS*, 436, 774
- Eldridge, J. J., Izzard, R. G., & Tout, C. A. 2008, *MNRAS*, 384, 1109
- Eldridge, J. J., & Tout, C. A. 2004, *MNRAS*, 353, 87
- Ensmann, L. M., & Woosley, S. E. 1988, *ApJ*, 333, 754
- Folatelli, G., Van Dyk, S. D., Kuncarayakti, H., et al. 2016, *ApJL*, 825, L22
- Fremming, C., Sollerman, J., Taddia, F., et al. 2016, *A&A*, 593, A68
- Gal-Yam, A. 2012, *Sci*, 337, 927
- Georgy, C., Ekström, S., Meynet, G., et al. 2012, *A&A*, 542, A29
- Graur, O., Bianco, F. B., Huang, S., et al. 2017, *ApJ*, 837, 120
- Habergan, S. M., Anderson, J. P., & James, P. A. 2010, *ApJ*, 717, 342
- Hachinger, S., Mazzali, P. A., Taubenberger, S., et al. 2012, *MNRAS*, 422, 70
- Hachisu, I., Matsuda, T., Nomoto, K., & Shigeyama, T. 1991, *ApJL*, 368, L27
- Hakobyan, A. A., Mamon, G. A., Petrosian, A. R., Kunth, D., & Turatto, M. 2009, *A&A*, 508, 1259
- Hakobyan, A. A., Nazaryan, T. A., Adibekyan, V. Z., et al. 2014, *MNRAS*, 444, 2428
- Hamann, W.-R., Koesterke, L., & Wessolowski, U. 1995, *A&A*, 299, 151
- Hammer, N. J., Janka, H.-T., & Müller, E. 2010, *ApJ*, 714, 1371
- Hamuy, M., Maza, J., Pinto, P. A., et al. 2002, *AJ*, 124, 417
- Hirai, R. 2017, *MNRAS*, 466, 3775
- Iwamoto, K., Nomoto, K., Höflich, P., et al. 1994, *ApJL*, 437, L115
- Kangas, T., Portinari, L., Mattila, S., et al. 2017, *A&A*, 597, A92
- Kelly, P. L., & Kirshner, R. P. 2012, *ApJ*, 759, 107
- Kifonidis, K., Plewa, T., Janka, H.-T., & Müller, E. 2003, *A&A*, 408, 621
- Kifonidis, K., Plewa, T., Scheck, L., Janka, H.-T., & Müller, E. 2006, *A&A*, 453, 661
- Kim, H.-J., Yoon, S.-C., & Koo, B.-C. 2015, *ApJ*, 809, 131
- Leloudas, G., Gallazzi, A., Sollerman, J., et al. 2011, *A&A*, 530, A95
- Liu, Y.-Q., Modjaz, M., Bianco, F. B., & Graur, O. 2016, *ApJ*, 827, 90
- Lucy, L. B. 1991, *ApJ*, 383, 308
- Lyman, J. D., Bersier, D., James, P. A., et al. 2016, *MNRAS*, 457, 328
- Maeda, K., Mazzali, P. A., Deng, J., et al. 2003, *ApJ*, 593, 931
- Maeda, K., Tanaka, M., Nomoto, K., et al. 2007, *ApJ*, 666, 1069

- Malesani, D., Fynbo, J. P. U., Hjorth, J., et al. 2009, *ApJL*, 692, L84
- Mao, J., Ono, M., Nagataki, S., et al. 2015, *ApJ*, 808, 164
- Maund, J. R. 2018, *MNRAS*, 476, 2629
- Maund, J. R., Wheeler, J. C., Patat, F., et al. 2007, *MNRAS*, 381, 201
- Mazzali, P. A., Maurer, I., Valenti, S., Kotak, R., & Hunter, D. 2010, *MNRAS*, 408, 87
- McClelland, L. A. S., & Eldridge, J. J. 2016, *MNRAS*, 459, 1505
- Meynet, G., & Maeder, A. 2005, *A&A*, 429, 581
- Modjaz, M., Li, W., Butler, N., et al. 2009, *ApJ*, 702, 226
- Müller, B., Gay, D. W., Heger, A., Tauris, T. M., & Sim, S. A. 2018, *MNRAS*, 479, 3675
- Nakar, E., & Piro, A. L. 2014, *ApJ*, 788, 193
- Nomoto, K., Yamaoka, H., Pols, O. R., et al. 1994, *Natur*, 371, 227
- Nugis, T., & Lamers, H. J. G. L. M. 2000, *A&A*, 360, 227
- Ono, M., Nagataki, S., Ito, H., et al. 2013, *ApJ*, 773, 161
- Paxton, B., Bildsten, L., Dotter, A., et al. 2011, *ApJS*, 192, 3
- Paxton, B., Cantiello, M., Arras, P., et al. 2013, *ApJS*, 208, 4
- Paxton, B., Marchant, P., Schwab, J., et al. 2015, *ApJS*, 220, 15
- Paxton, B., Schwab, J., Bauer, E. B., et al. 2018, *ApJS*, 234, 34
- Piro, A. L., & Nakar, E. 2013, *ApJ*, 769, 67
- Podsiadlowski, P., Joss, P. C., & Hsu, J. J. L. 1992, *ApJ*, 391, 246
- Prentice, S. J., & Mazzali, P. A. 2017, *MNRAS*, 469, 2672
- Prentice, S. J., Mazzali, P. A., Pian, E., et al. 2016, *MNRAS*, 458, 2973
- Reilly, E., Maund, J. R., Baade, D., et al. 2016, *MNRAS*, 457, 288
- Richmond, M. W., van Dyk, S. D., Ho, W., et al. 1996, *AJ*, 111, 327
- Sanders, N. E., Soderberg, A. M., Levesque, E. M., et al. 2012, *ApJ*, 758, 132
- Sauer, D. N., Mazzali, P. A., Deng, J., et al. 2006, *MNRAS*, 369, 1939
- Shigeyama, T., Nomoto, K., Tsujimoto, T., & Hashimoto, M.-A. 1990, *ApJL*, 361, L23
- Shivvers, I., Modjaz, M., Zheng, W., et al. 2017, *PASP*, 129, 054201
- Smith, N., Li, W., Filippenko, A. V., & Chornock, R. 2011, *MNRAS*, 412, 1522
- Soderberg, A. M., Berger, E., Page, K. L., et al. 2008, *Natur*, 453, 469
- Stritzinger, M., Hamuy, M., Suntzeff, N. B., et al. 2002, *AJ*, 124, 2100
- Stritzinger, M. D., Taddia, F., Burns, C. R., et al. 2018, *A&A*, 609, A135
- Swartz, D. A. 1991, *ApJ*, 373, 604
- Taddia, F., Sollerman, J., Leloudas, G., et al. 2015, *A&A*, 574, A60
- Taddia, F., Stritzinger, M. D., Bersten, M., et al. 2018, *A&A*, 609, A136
- Tanaka, M., Kawabata, K. S., Hattori, T., et al. 2012, *ApJ*, 754, 63
- Tanaka, M., Kawabata, K. S., Maeda, K., Hattori, T., & Nomoto, K. 2008, *ApJ*, 689, 1191
- Tanaka, M., Maeda, K., Mazzali, P. A., Kawabata, K. S., & Nomoto, K. 2017, *ApJ*, 837, 105
- Tauris, T. M., Langer, N., & Podsiadlowski, P. 2015, *MNRAS*, 451, 2123
- Tsvetkov, D. Y., Blinnikov, S. I., & Pavlyuk, N. N. 2001, *AsTL*, 27, 411
- Valenti, S., Elias-Rosa, N., Taubenberger, S., et al. 2008, *ApJL*, 673, L155
- Valenti, S., Fraser, M., Benetti, S., et al. 2011, *MNRAS*, 416, 3138
- van den Bergh, S., Li, W., & Filippenko, A. V. 2005, *PASP*, 117, 773
- Van Dyk, S. D., Zheng, W., Brink, T. G., et al. 2018, *ApJ*, 860, 90
- Wellstein, S., & Langer, N. 1999, *A&A*, 350, 148
- Wheeler, J. C., Yi, I., Höflich, P., & Wang, L. 2000, *ApJ*, 537, 810
- Wongwathanarat, A., Janka, H.-T., Müller, E., Pllumbi, E., & Wanajo, S. 2017, *ApJ*, 842, 13
- Woosley, S. E. 1993, *ApJ*, 405, 273
- Woosley, S. E., & Bloom, J. S. 2006, *ARA&A*, 44, 507
- Woosley, S. E., & Eastman, R. G. 1997, in *NATO Advanced Science Institutes (ASI) Series C*, Vol. 486 ed. P. Ruiz-Lapuente, R. Canal, & J. Isern (Dordrecht: Kluwer), 821
- Woosley, S. E., Langer, N., & Weaver, T. A. 1995, *ApJ*, 448, 315
- Xiao, L., & Eldridge, J. J. 2015, *MNRAS*, 452, 2597
- Yamanaka, M., Nakaoka, T., Tanaka, M., et al. 2017, *ApJ*, 837, 1
- Yoon, S.-C. 2015, *PASA*, 32, e015
- Yoon, S.-C. 2017, *MNRAS*, 470, 3970
- Yoon, S.-C., Dessart, L., & Clocchiatti, A. 2017, *ApJ*, 840, 10
- Yoon, S.-C., Gräfener, G., Vink, J. S., Kozyreva, A., & Izzard, R. G. 2012, *A&A*, 544, L11
- Yoon, S.-C., Woosley, S. E., & Langer, N. 2010, *ApJ*, 725, 940